Available online at www.sciencedirect.com
ScienceDirect
Earth and Planetary Science Letters 259 (2007) 66–76
EPSL
www.elsevier.com/locate/epsl

Deep upper-mantle melting beneath the Tasman and Coral Seas detected with multiple *ScS* reverberations

Anna M. Courtier *, Justin Revenaugh

Department of Geology and Geophysics, University of Minnesota, 310 Pillsbury Drive SE, Minneapolis, MN 55455, USA

Received 14 November 2006; received in revised form 19 April 2007; accepted 20 April 2007
Available online 4 May 2007
Editor: R.D. van der Hilst

Abstract

Multiple *ScS* reverberations are used to search for mantle reflectors beneath the Tasman and Coral Seas with a hierarchical waveform-inversion/migration method. In addition to the major transition zone discontinuities, a low-velocity layer above the 410-km discontinuity is detected. The top of the low-velocity layer lies at an average depth of 352 km, indicating that the layer could be more than 70-km thick if it persists to the 410-km discontinuity, which occurs at an average depth of 420 km along paths containing the low-velocity layer. We attribute the low velocities to partial melt resulting from volatile-induced melting. The considerable thickness of the partial melt layer may require thin films of a hydrous melt with a zero-degree dihedral angle surrounding grains or the combined effect on melting of the addition of both water and carbon to the deep upper mantle via subduction. Although the depths of the transition zone discontinuities do not indicate that the transition zone itself is rich in water, the impedance contrasts do contain a subtle signature that could be related to transition zone water, namely a decrease in the impedance contrast across the 410-km discontinuity and a relatively strong 520-km discontinuity.

Keywords: mantle; transition zone; discontinuities; partial melting; water; low-velocity zone

1. Introduction

Theoretical and experimental studies predict melting associated with the addition of volatiles such as water or carbon dioxide to mantle rocks in the deep upper mantle under a variety of conditions (Bercovici and Karato, 2003; Dasgupta et al., 2004; Dasgupta and Hirschmann, 2006; Karato et al., 2006), however the density, buoyancy, and longevity of these melts at depth is debated (Stolper et al., 1981; Ohtani et al., 1995; Leahy and Bercovici, in press). Several seismic studies have documented low-velocity layers or regions in the deep upper mantle that can be interpreted as localized layers of partial melt (Revenaugh and Sipkin, 1994; Vinnik and Farra, 2002; Vinnik et al., 2003; Song et al., 2004). If melt is the cause of lowered velocities, then either the melt is dense enough to accumulate and persist in the region or the signature of an earlier melting episode in the deep upper mantle remains seismically detectable.

While the majority of water carried by subducted slabs dehydrates and is lost in the uppermost 200-km of the mantle (Tatsumi, 1989; Irifune et al., 1998), small amounts of water may be carried into the deep upper mantle and transition zone by dense hydrous magnesium silicates (e.g., Shieh et al., 1998) or in nominally

* Corresponding author. Tel.: +1 612 624 8557; fax: +1 612 625 3819.
E-mail address: cour0090@umn.edu (A.M. Courtier).

0012-821X/$ - see front matter © 2007 Elsevier B.V. All rights reserved.
doi:10.1016/j.epsl.2007.04.027

anhydrous minerals (e.g., Katayama and Nakashima, 2003). If the slab stalls near the 660-km discontinuity (e.g., Anderson, 1989; Irifune and Ringwood, 1993), it will warm and may release volatiles in the transition zone (Irifune et al., 1998). This water may concentrate in the transition zone due to its enhanced solubility in transition zone minerals over minerals above and below (Kohlstedt et al., 1996; Bolfan-Casanova et al., 2000; Murakami et al., 2002; Hirschmann et al., 2005). The transition zone water filter hypothesis (Bercovici and Karato, 2003; Karato et al., 2006) predicts a layer of hydrous melt in the deep upper mantle resulting from hydrous material upwelling through a "water-rich" transition zone into the overlying upper mantle. Since the upper mantle mineral assemblage has lower water solubility than that of the transition zone (Kohlstedt et al., 1996; Hirschmann et al., 2005), the upwelling material can become saturated and melt. In this scenario, a layer of melt is expected to accumulate atop the 410-km discontinuity, directly above the mantle transition zone. Revenaugh and Sipkin (1994) proposed volatile-induced melting to explain a low-velocity layer above the transition zone below the Sea of Japan and eastern China. In their hypothesis, volatile induced melt forms in the upper mantle and then sinks to the 410-km discontinuity due to negative buoyancy, slab entrainment, or some combination of the two. Unlike the water-filter hypothesis, this scenario does not require upwelling of material from below the region of accumulated melt, but may require unrealistically high melt density.

Since water is incorporated differently into the structures of nominally anhydrous upper mantle, transition zone, and lower mantle minerals (Bell and Rossman, 1992; Kohlstedt et al., 1996; Ingrin and Skogby, 2000; Bolfan-Casanova et al., 2000, 2003, 2005), it has a signature in the pressure–temperature stability fields of the phase changes producing the major transition zone discontinuities at 410, 520, and 660 km depth, affecting both the equilibrium depth and the impedance contrast of the seismic discontinuities. The 410-km discontinuity is broadened (Akaogi et al., 1989; Wood, 1995; Helffrich and Wood, 1996; Smyth and Frost, 2002) and migrates to shallower depths (Chen et al., 2002; Smyth and Frost, 2002) under hydrous conditions. The 660-km discontinuity also broadens under the influence of water (Ito and Takahashi, 1989; Higo et al., 2001), but occurs at deeper depths than when dry (Higo et al., 2001). The transition across the 520-km discontinuity narrows in the presence of water (Inoue et al., 1998).

The effect of carbon on melting in the deep upper mantle may be similar to that of water stored in nominally anhydrous minerals (e.g., Dalton and Presnall, 1998; Dasgupta et al., 2004; Dasgupta and Hirschmann, 2006). Studies investigating the relationship between upper mantle melting and carbon dioxide have examined a range of rock compositions and pressure–temperature conditions. While the early studies focused on the relationship of carbon with shallow upper mantle low-velocity zones (e.g., Green, 1972; Eggler, 1976; Wyllie and Huang, 1976), more recent studies have examined conditions nearing the of the upper mantle as well (Dalton and Presnall, 1998; Dasgupta et al., 2004; Dasgupta and Hirschmann, 2006). Dalton and Presnall (1998) experimentally determined the coexistence of carbonatite melt with lherzolite. While carbonatites are rare on Earth's surface, they concluded that carbonatites could be abundant within the upper mantle. Dasgupta et al. (2004) and Dasgupta and Hirschmann (2006) conducted experiments under deep upper mantle conditions to examine melting caused by carbon dioxide in eclogite and peridotite. Carbonate minerals survive in nominally anhydrous eclogite to deep upper mantle and/or transition zone conditions. Upon assimilation into the convecting upper mantle, upwelling carbonated eclogite releases melt beginning around 400 km depth and continues to coexist as eclogite plus melt until ~280 km (Dasgupta et al., 2004). Melting of upwelling carbonated peridotite occurs as deep as 330 km under ridge conditions (Dasgupta and Hirschmann, 2006). Since carbon dioxide is incorporated into the major mantle minerals in only very small amounts (on the order of <1 ppm by weight; Keppler et al., 2003), the presence of carbon should not be manifest in discontinuity depth or impedance contrast across the transition zone discontinuities.

The stability and steady-state thickness of a partial melt layer is debated. Seismic studies detecting layers up to 100 km in thickness and consistent with the velocity decrements of partial melt (e.g., Revenaugh and Sipkin, 1994; Song et al., 2004) are at odds with numerical calculations suggesting that these layers must be thin. Hirschmann et al. (2006) considered the stability of a layer of hydrous melt from a phase-equilibria standpoint and concluded that the melt layer would not exceed a thickness of ~7 km. From the fluid dynamics perspective, this layer might not exceed even a few meters thickness before collapsing due to insufficient surface tension (Stevenson, 1986) or by recirculation into the transition zone via slab or viscous entrainment (Leahy and Bercovici, in press). However, the melt layer calculated by Leahy and Bercovici (in press) was modeled as a layer composed of 100% melt that compacted due to gravitational collapse rather than a thicker region of partial melt. Due to this and other model simplifications, their model provides better

constraints with respect to the lateral extent of the melt layer rather than melt layer thickness. Regardless of the thickness of the melt layer, small amounts of melt may remain along grain edges even after the bulk of partial melt has been extracted, leaving a signal that melt has passed through a region and, under the right flow conditions, producing a thick region of melt-modified mantle (Hier-Majumder et al., 2006).

Melt distribution and interconnectivity are controlled by the dihedral angle (θ) of the melt in contact with the surrounding solids. For dihedral angles of $0° < \theta \leq 60°$, melt will be distributed in pockets at grain triple junctions (e.g., Bulau et al., 1979). Complete grain boundary wetting in the form of a melt film surrounding individual grains may occur if the dihedral angle is 0° (Smith, 1964). This would allow even very small amounts of melt to remain interconnected over a broad depth range and would enhance seismic detection of the melt. In addition to a larger shear wave velocity decrement resulting from interconnected melt, the spatial distribution of interconnected melt is broader relative to a region composed of individual melt pockets (Blackman and Kendall, 1997). Experimental work with partially molten peridotite finds dihedral angles of 0–10° for large grain size and low melt fraction (Cmiral et al., 1998), and the dihedral angle of hydrous silicate melt with olivine goes to 0° at pressures above 7–8 GPa (Yoshino et al., 2007). Despite a dihedral angle of 25–30°, interconnectivity of carbonated mantle melts is also likely, even for very low melt fractions (Minarik and Watson, 1995).

Seismic observations of low-velocity zones in the deep upper mantle have been limited to regions of subduction (Revenaugh and Sipkin, 1994; Pino and Helmberger, 1997; Song et al., 2004 this study) or to regions associated with continental flood basalts (Vinnik and Farra, 2002; Vinnik et al., 2003). Revenaugh and Sipkin (1994) detected a low-velocity layer beneath eastern China and the Sea of Japan at a depth of approximately 330 km and with a thickness of ~50–100 km. A similar feature was detected in the northwestern United States by Song et al. (2004), who reported a low-velocity layer located directly atop the 410-km discontinuity that varied in thickness over short length-scales, ranging between 20 and 90 km thick. In both cases, the velocity decrement was attributed to a compositional anomaly due to the presence of volatiles that may have been introduced to the region by subduction. Pino and Helmberger (1997) report a feature in a similar depth range that can be explained equally well by a 410-km discontinuity elevated to 368 km or a low velocity layer confined between 318 and 368 km depth. This feature occurs in the West Mediterranean Basin, a region influenced by subduction of the African Plate. Deep low velocity zones away from subduction zones have been attributed to hydrated mantle material beneath overlying dry cratonic roots in regions also associated with continental flood basalts (Vinnik and Farra, 2002; Vinnik et al., 2003).

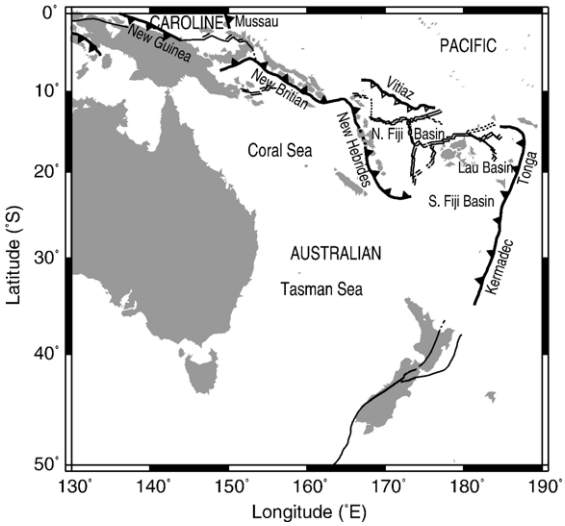

Fig. 1. General tectonic map of the southwest Pacific region. Solid triangles indicate present-day subduction polarity. Open triangles indicate polarity of past subduction along the Vitiaz trench. Double lines are ridges; solid lines are transform faults.

Revenaugh and Jordan (1991b,c) investigated the upper mantle and transition zone structure of the southwest Pacific and did not model a low-velocity zone in the deep upper mantle. However, the seismic signature of this layer is subtle, and closer inspection of their reflectivity profiles (e.g., Corridor #5 in Revenaugh and Jordan, 1991c) indicates that the layer may be present but obscured due to averaging along long and variable or broad source–receiver corridors. We utilize nearly twenty years of additional seismicity and the much greater present-day receiver density in the region to re-examine discontinuity structure beneath the southwest Pacific. The increase in available data allows us to narrow the geographic area covered by individual source–receiver corridors, reducing averaging, enabling detection of subtle features, and increasing the likelihood of highlighting localized features that may go undetected in smaller *ScS* datasets. The geometry of the subduction in the study area produces a broad earthquake source array that allows for a large number of source–receiver paths. This, in turn, allows us to study the mantle beneath specific geologic regions rather than averaging over a variety of terrains.

The southwest Pacific region is bounded by Australia to the west, Papua New Guinea, the Solomon Islands and

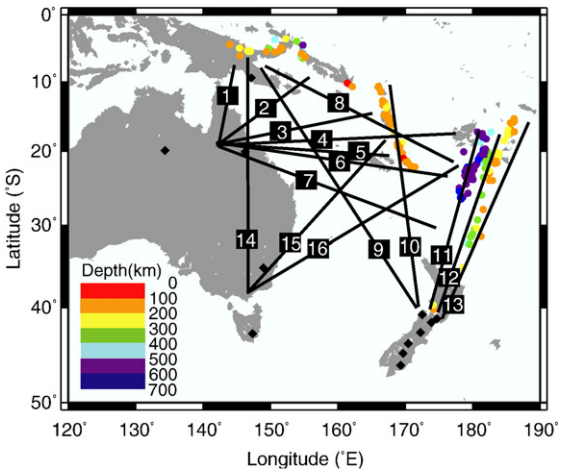

Fig. 2. Map of study area with source–receiver paths connecting events (circles) and seismic stations (diamonds). Paths are grouped according to receiver region and are numbered in a clockwise direction. Events are color coded according to depth.

the Vitiaz Trench to the north, the Tonga–Kermadec trench to the east, and New Zealand and Tasmania to the south (Fig. 1). Subduction occurs along the northern and eastern boundaries. The Caroline plate is subducting under the Australian plate along the New Guinea trench (Hall and Spakman, 2003). Further east, subduction vergence reverses, with the Australian plate subducting beneath the Pacific plate at the New Britain trench along the Solomon Islands and the New Hebrides trench along the Vanuatu chain (Hall and Spakman, 2003; Sdrolias et al., 2003), which is undergoing trench roll-back, allowing the opening of the North Fiji Basin (Auzende et al., 1994). Subduction polarity is reversed along the eastern boundary, where the Pacific plate subducts beneath the Australian plate along the Tonga–Kermadec trench (Sdrolias et al., 2003). Extension occurs to the west of and parallel to this trench, creating the Lau Basin (Parson and Wright, 1996; Taylor et al., 1996).

2. Data

We conducted a study of the transition zone and upper mantle beneath the Tasman and Coral Seas to investigate mantle heterogeneity in a region heavily influenced by subduction, a process that makes the area a likely candidate for locally-enhanced thermal and chemical heterogeneity. We modeled mantle discontinuities using the hierarchical waveform-inversion method of Revenaugh and Jordan (1991a,b) on multiple *ScS* reverberations from nearly 180 intermediate and deep-focus earthquakes captured at 12 stations of the DWWSSN, GEOFON, GEOSCOPE, IDA, NZSE (PASSCAL), and USGS networks. Earthquakes included in the study have magnitude $m_b > 5.0$, depth $z > 75$ km, and occurred between 1977 and 2003. Source parameters for each of the events are reported in the Supplementary data.

Seismograms were rotated, deconvolved to ground velocity, and decimated to a three-second sampling interval. All seismograms were run through a cosine-squared zero-phase bandpass filter between 8 and 60 mHz, with filter corners at 10 and 45 mHz. Seismograms with low signal-to-noise ratios or apparent source time–function complexity were discarded prior to modeling. The remaining transverse-component seismograms were divided into sixteen source–receiver corridors containing a minimum of five seismograms each. Corridors were determined with regard to tectonic setting and data density (Fig. 2). A representative seismogram is shown in Fig. 3.

3. Method

The hierarchical waveform inversion/migration method of Revenaugh and Jordan (1991a,b) was used to model zeroth- and first-order *ScS* reverberations. Zeroth-order *ScS* reverberations are multiple *ScS* and *sScS* phases; first-order reverberations are similar but are reflected once from a mantle discontinuity along the path

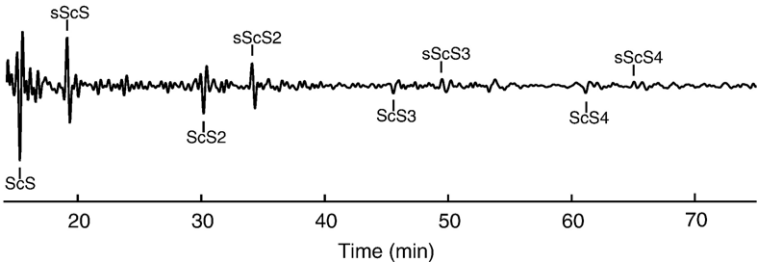

Fig. 3. Long period, SH-polarized seismogram of the October 22, 2002 earthquake (20.633° S, 178.391° W, 546 km depth) recorded at station CTAO (20.088° S, 146.255° E) with multiple *ScS* phases within the reverberative interval labeled.

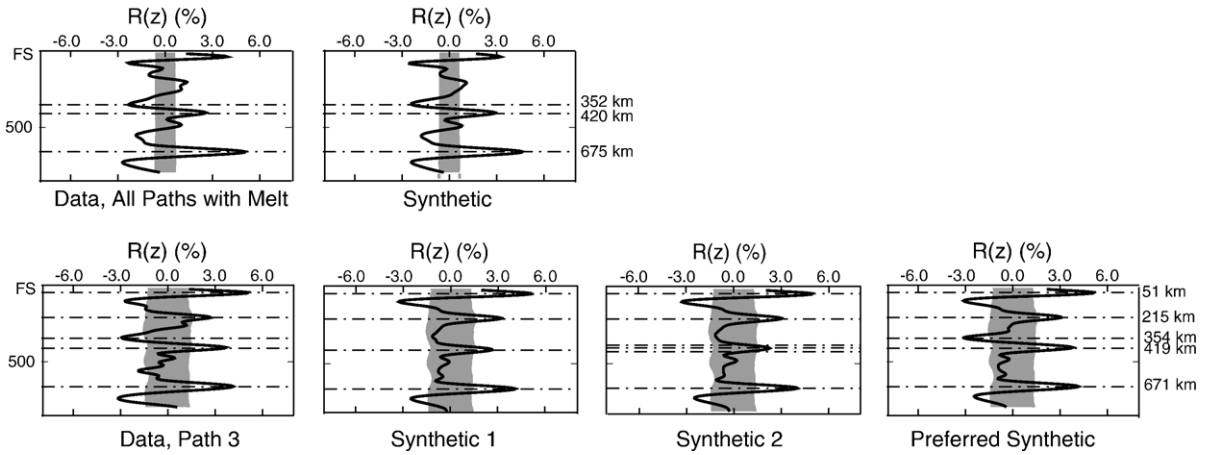

Fig. 4. SH impedance reflectivity profile for source–receiver corridors that contained observations of a low-velocity layer above the 410-km discontinuity. Vertical axis is depth (km) from the free surface (FS); horizontal axis is reflection coefficient ($R(z)$, %). Upper: composite SH impedance reflectivity profile for all of the source–receiver corridors that contained observations of a low-velocity layer above the 410-km discontinuity. The reflector depths shown by dashed lines were included in every model in the stack. Lower: representative individual SH impedance reflectivity profile from Path 3 connecting Vanuatu and Northern Australia. Center panels show profiles without the melt layer modeled for a sharp interface (Synthetic 1) and a gradient (Synthetic 2) at the 410-km discontinuity. Depths for reflectors included in the preferred model are shown by dashed lines.

between the source and receiver. A minimum of two ScS_n–$sScS_n$ pairs were modeled for each seismogram, extending to a maximum of four pairs ($n=1$–4) for traces with a high signal-to-noise ratio and minimal interference from other arrivals. The synthetic zeroth-order reverberations were stripped from the data, producing a residual signal populated by first- and higher-order reverberations, noise, and minor residual energy from the zeroth-order reverberations (Revenaugh and Jordan, 1989). One-dimensional migration of the first-order reverberations (Revenaugh and Jordan, 1991b) yields a radial profile of SH-reflectivity in the mantle. The folding of many seismograms (and thus many more reverberations) into a single depth profile makes possible the identification of low amplitude reflections and variations in waveform shape that would be difficult, if not impossible in some cases, to discern on individual seismograms. For this reason, we model the reflectivity profiles, not individual seismograms. To do this, synthetic seismograms are migrated in a series of iterations to produce a synthetic reflection profile closely matching the data profile while containing the fewest number of discontinuities necessary. The generic velocity model of Revenaugh and Jordan (1991a) used in the migration was scaled to match the *ScS* travel time for each source–receiver corridor. In what follows, discontinuity depth is referenced to PREM (Dziewonski and Anderson, 1981) after path-specific corrections for bathymetry, crustal thickness, and background mantle heterogeneity are applied following Revenaugh and Jordan (1991b).

4. Results

Corrected discontinuity depths and apparent impedance contrasts for each of the source–receiver corridors

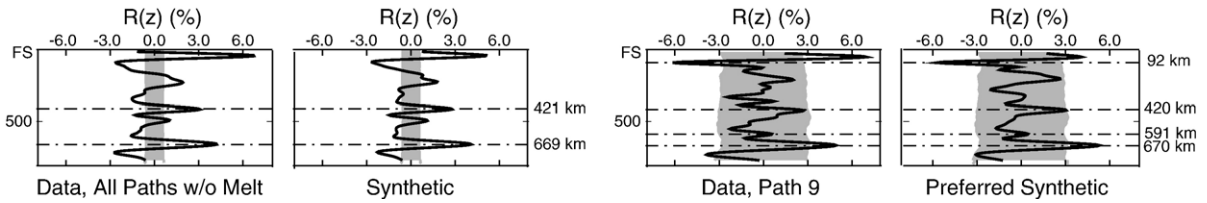

Fig. 5. SH impedance reflectivity profile for source–receiver corridors that did not contain observations of a low-velocity layer above the 410-km discontinuity. Conventions are the same as in Fig. 4. Left: composite SH impedance reflectivity profile for all of the source–receiver corridors that did not contain observations of a low-velocity layer above the 410-km discontinuity. Right: representative individual SH impedance reflectivity profile from Path 9 connecting Papua New Guinea and New Zealand.

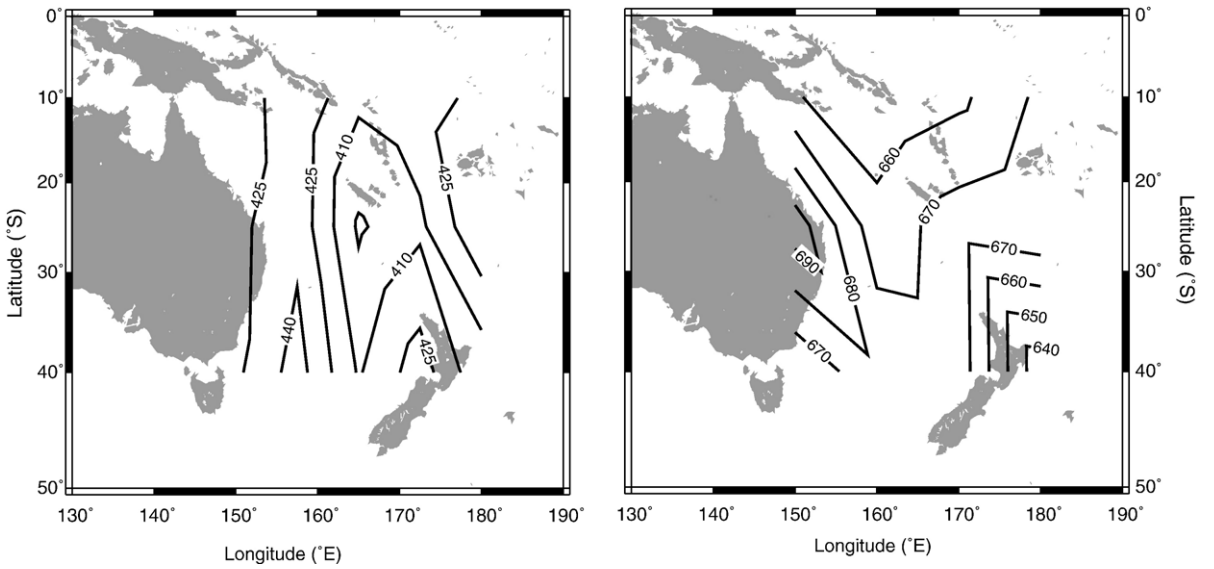

Fig. 6. Modeled topography along the 410-km (left) and 660-km (right) discontinuities. After applying a delete-one jack-knife outlier test to the dataset, Paths 1 and 14 have been omitted from the topography model for the 410-km and 660-km discontinuities, respectively.

are reported in the Supplementary data. Representative SH-reflectivity profiles for the study area are shown in Figs. 4 and 5. Profiles are partitioned into those that require a low-velocity layer above the 410-km discontinuity to match the data and those that do not. For profiles that do require the low-velocity layer, intermediate synthetics without the layer modeled are also shown in Fig. 4. Cases with both a sharp interface and a gradient across the 410-km discontinuity were considered. Due to the frequency of the *ScS* reverberations, the data are not highly sensitive to changes in discontinuity structure and are agnostic with regards to transition intervals less than ~20 km. Other seismic methods (e.g., Van der Meijde et al., 2005) can provide these constraints but have not been applied to this study area. In addition to the low-velocity layer and transition zone discontinuities at average depths of 421 km, 515 km, and 672 km, several paths contained additional discontinuities in the shallow upper mantle.

The Hales discontinuity (H; see Revenaugh and Jordan (1991c) for discontinuity nomenclature) is seen intermittently and with depths varying between 40 and 115 km in paths across the northern part of the study area but appears more consistently in the southern half of the region, with depth variability limited between 50 and 60 km. Inconsistency in the northern region may be related to incomplete modeling of crustal structure, which can lead to artifacts in the reflectivity profile for the uppermost mantle (and lowermost mantle due to the inherent ambiguity of first-order reverberations that include at least one core reflection). Corridors located primarily in the central region of the study area detect the Gutenberg discontinuity (G) at depths varying between 80 and 150 km. This discontinuity is characterized by a strong negative impedance contrast, typically associated with the detection of asthenosphere beneath oceanic areas (Revenaugh and Jordan, 1991c). Because of migration ambiguity, it is possible that some portion of the signal assigned to G stems from a discontinuity in D″ with a positive shear-wave impedance contrast, a feature that has been detected within the study area by Neuberg and Wahr (1991) and Kendall and Shearer (1995). The Lehmann discontinuity (L) may be present in two segments; an eastern segment at an average depth of approximately 222 km and focused beneath the Tonga–Kermadec trench and a western segment at an average of 236 km depth and constrained to lie beneath the Coral Sea in the northwest corner of the study area. An observation in this depth range is also present in the preferred model for Path 15, but the apparent impedance contrast is weaker than all of the other observations of L, and since it is not required in the models for neighboring corridors, we regard this feature as speculative.

Path-averaged discontinuity depths from individual source–receiver corridors were converted into a two-dimensional grid using a simple smoothed least squares inverse and assuming equal weighting of all reverberation interactions with the reflector (Fig. 6). We used the Akaike Information Criteria (AIC) to determine the optimum grid size (Akaike, 1974). For the 410-km, this resulted in grid centers separated by 15° in latitude and

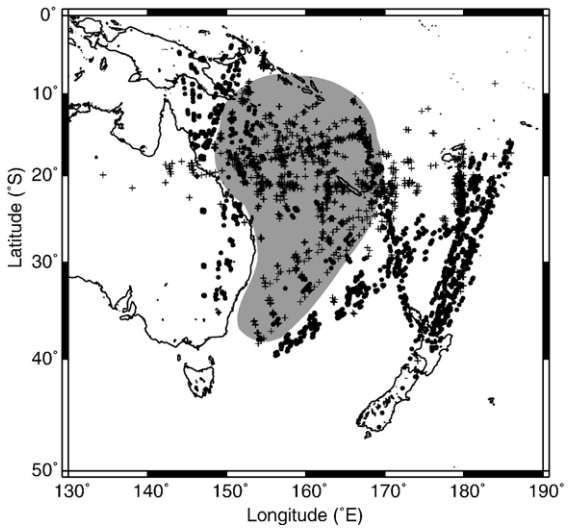

Fig. 7. Inferred lateral extent (shaded area) of the low-velocity layer observed in the deep upper mantle. Symbols plotted are surface bounce points of multiple *ScS* phases for individual traces. Crosses indicate traces belonging to paths that did require the low-velocity layer in the preferred reflectivity profile; circles indicate traces belonging to paths that did not. Crosses that fall outside of the shaded area result from along-path averaging.

7.5° in longitude; for the 660-km discontinuity, grid centers were spaced at 15° latitude and 10° longitude increments. The geographic locations of *ScS* surface bounce points and discontinuity depth observed within each corresponding source–receiver path were used as data points contributing to the depth estimates at each grid center. Data were not shared between grid cells. The grid cells resulting from the AIC are larger than the effective Fresnel zone, which was determined by calculating ScS_2 travel times for raypaths with perturbations in the location of the surface bounce point. Results for first-order reverberations and reverberations with more core bounces are similar. Because raypaths are close to vertical in the upper mantle, perturbations of the surface reflection point along the great circle and perpendicular to it produce similar delays. As a result, the effective Fresnel Zone (defined as the geographic limit of sampling within one quarter of the dominant period) is well approximated by a 5° circular cap. Additional source receiver paths crossing the study area would be required to resolve structures on the scale of the Fresnel zone. The topography resulting from the AIC and resulting least squares inversion represents the combination of highest resolution and highest confidence available with the dataset. A delete-one jack-knife outlier test was applied to each discontinuity dataset to examine contributions of individual source–receiver paths to the modeled topography. The results shown in Fig. 6 omit Path 1 for the 410-km discontinuity and Path 14 for the 660-km discontinuity. These paths contributed a disproportionate amount to the model and lead to apparent artifacts in the topography. Both paths are located along the western boundary of the study area and large portions of each are not crossed by other paths, allowing them to dominate sampling locally and produce a highly smeared result. While not suited for inclusion in the inversions, path-averaged results for Paths 1 and 14 are considered reliable. The topography shown along the 410-km and 660-km discontinuities in Fig. 6 provides a reasonable fit to our data with few degrees of freedom. However it is possible, likely in fact (e.g., Gilbert et al., 2003), that smaller scale topography exists beneath the region.

Topography along both the 410-km and 660-km discontinuities exceeds the errors on discontinuity depth of 5–7 km (Revenaugh and Jordan, 1989) but is not correlated between the two discontinuities for results from individual source–receiver paths or for results from the least-squares inversion. The 410-km discontinuity lies at an average depth of 421 km, within error of the global mean (418 km; Flanagan and Shearer, 1998), but is 5–10 km deeper than the local observations for the area of Flanagan and Shearer (1998). The 660-km discontinuity has an average depth of 672 km across the study area, which is similar to local observations from

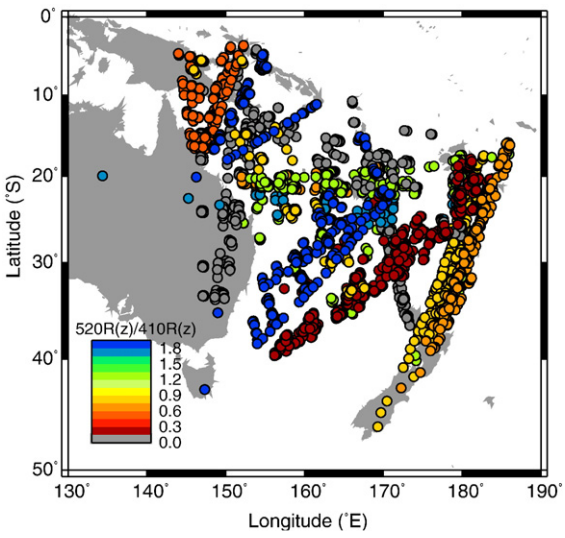

Fig. 8. Path-averaged ratios of impedance contrast for the 520-km discontinuity to the 410-km discontinuity. Symbols plotted are surface bounce points of multiple *ScS* phases for individual traces. A ratio of zero (gray circles) indicates that the 520-km discontinuity was not observed in the corridor.

Flanagan and Shearer (1998) and deeper than the global mean (660 km). Results obtained from the inversion (Fig. 6) show saddle-shaped topography along the 410-km discontinuity, with a broad topographic high running north–south through the center of the study area and deeper observations near the Tonga–Kermadec trench and the Australian continent. The 660-km discontinuity is also deeper near Australia relative to the rest of the study area, whereas it is relatively flat across the Coral and Tasman Seas and slightly shallower toward New Zealand.

The low-velocity layer above the transition zone occurs at an average depth of 352 km and is centered beneath the Coral Sea, but extends to the northernmost Tasman Sea. The paths that show the layer provide a rough geographic definition of the extent of the layer (Fig. 7). From these, it appears to extend more than 20° along both the north–south and east–west directions, but, because of path-averaging and a limited catalog of paths limning the region, the layer may be as much as 5° smaller or larger along one or both directions. We did not attempt to resolve geographic variability in the depth to the top of the low-velocity layer. This decision was premised on the smaller number of paths with this feature relative to paths containing the 410-km and 660-km discontinuities and because the modeled depth of the feature is heavily influenced by strong interference with the larger 410-km discontinuity, leading to a larger uncertainty of path-averaged depth (±15 km).

The presence of the low-velocity layer is associated with a decrease in the impedance contrast across the 410-km discontinuity and a relatively strong 520-km discontinuity (Fig. 8). The average thickness of the layer is ~70 km; the minimum observed thickness of ~40 km is close to the minimum resolution threshold of the multiple *ScS* reverberations (~25 km), and it is possible that the layer exists along other paths but is too thin to resolve or too weak to detect.

5. Discussion

The lateral extent of the low-velocity layer (Fig. 7) coincides with a 520-km discontinuity with impedance contrast enhanced relative to the 410-km discontinuity (Fig. 8), which has been interpreted as an indication of a water-enriched transition zone in both laboratory and seismic studies (Inoue et al., 1998; Van der Meijde et al., 2005; Courtier and Revenaugh, 2006). While the ratios of impedance contrast between the 520-km and 410-km discontinuities are not as large in this study as in those just mentioned, we interpret them as a signal, albeit subtle, of transition zone water and incorporate this into our discussion of the overlying low-velocity layer.

Laboratory experiments demonstrate that water-induced melting above the transition zone can occur under hydrous conditions due to the difference in water solubilities of olivine and wadsleyite (e.g., Kohlstedt et al., 1996; Chen et al., 2002). Such melting is an integral aspect of the transition zone water filter hypothesis (Bercovici and Karato, 2003; Karato et al., 2006), and if it occurs extensively could profoundly impact the chemical evolution of the mantle.

The density of hydrous silicate melt is intermediate between upper mantle and transition zone minerals for ranges of water and iron contents and temperatures (Matsukage et al., 2005; Sakamaki et al., 2006), and so stable hydrous melt layers rooting on the 410-km discontinuity are feasible with regard to density. Numerical studies, however, suggest that a hydrous melt layer may not exceed a few meters (Leahy and Bercovici, in press) to a few kilometers in thickness (Hirschmann et al., 2006). It may be reasonable to expand the lower limit of a few meters (Leahy and Bercovici, in press) to the order of kilometers if the compacted melt layer modeled is distributed as a partial melt layer with low melt fraction. The latter constraint, based on the pressure interval of the olivine to wadsleyite transition under saturated conditions (and thus with partial melting), applies only to the thickness of the melt-producing region, not the resulting melt "pool." All the same, neither limit compares well with the ~70 km mean thickness observed in this study, assuming the layer extends to the 410-km discontinuity. We propose three solutions to this problem.

The first solution hinges on the distribution of melt in the matrix. A dihedral angle of 0° has been observed for silicate melt in contact with olivine–basalt aggregates (Cmiral et al., 1998) and with olivine at pressures above 7–8 GPa (Yoshino et al., 2007). Zero degree dihedral angles allow a thin film of melt to nearly completely surround grain boundaries. Surface tension counteracts the melt's negative buoyancy, enabling the partial melt layer to be much thicker (Hier-Majumder et al., 2006). In addition, Hier-Majumder et al. (2006) also describe capillary action in the melt that leads to the retention of small amounts of melt after upwelling (or downwelling) and passage of melt through a region, producing a "wake" of melt pockets. The melt films and remnant melt pockets expand the region influenced by partial melting. Whether or not they are able to produce the ~70-km thick layers we observe is uncertain at this juncture. Also uncertain is the ability of remnant pockets to produce the needed velocity decrement, which is on the order of 5%.

Under this scenario, the rapid change in shear-wave impedance near 350 km implies that the dihedral angle of the melt becomes greater than 0° at this point. This transition would cause any melt above 350 km depth to be localized in pockets at grain triple junctions rather than as a film surrounding grains. This distribution would mute the seismic signature of small melt fractions, making it more or less transparent. The surface tension of melt with a larger dihedral angle would also lead to melt separation (Hier-Majumder et al., 2006) and descent if it remains negatively buoyant.

Although water solubility in olivine increases with pressure (Kohlstedt et al., 1996), varying water solubilities in other mantle minerals may produce a local maximum in water storage capacity near 350 km (Hirschmann et al., 2005). If this is correct and if melt is responsible for the low velocity layer, it must either accumulate up to this point or percolate down to it. If there is no local maximum, but rather a gradual increase in water solubility with depth approaching the 410-km discontinuity, then upward advection of mantle mass through the wadsleyite–olivine transition with water weight percentage below the storage capacity at 410 km would not immediately induce melting. Continued upward advection, and gradual reduction of water solubility, could result in melting significantly above the 410-km discontinuity. Under this model, the negative impedance reflector near 350 km depth marks the onset of melting in ascending mantle. Lowered velocities beneath could be due to an accumulation of negatively buoyant melt or remnants of melt produced by more water-rich ascending mantle rock.

A third possibility involves carbon. Since carbon is not incorporated into the major mantle minerals (Keppler et al., 2003), melting induced solely by carbon is not consistent with the observed linkage of low-velocity layer occurrence and impedance contrasts across the 410-km and 520-km discontinuities. However, it is possible that water and carbon conspire to induce melting over a broader region in the deep upper mantle.

Carbonate minerals are introduced to the deep upper mantle via subduction of carbonated eclogite. Subsequent upwelling of the material leads to melting between 280 and 400 km (Dasgupta et al., 2004). Unlike hydrous melts, carbonated melts are less dense than typical upper mantle mineral assemblages (Dobson et al., 1996). Water is very soluble in carbonate melts (Keppler, 2003), and mixing of hydrous melt into carbonated melts produced above the transition zone could counteract the negative buoyancy of hydrous melts. Ascent of the hydrous-carbonate melt along with continued carbonated mantle melting could produce a thick layer of partial melt in the deep upper mantle.

The top of the low-velocity layer beneath the Coral and Tasman Seas lies at an average of 352 km below the surface. If due to carbonate-catalyzed melt, this depth represents either the upward limit of the melt's ascent toward the surface or a crossover in the relative buoyancy of hydrous carbonated melt and ambient mantle. Given the paucity of laboratory constraints on the properties of hydrous-carbonate melts and the low density (Dobson et al., 1996) and high interconnectivity of carbonate melts (Minarik and Watson, 1995), we favor the former, but clearly more work is needed.

6. Conclusions

Extensive regions of partial melting in the deep upper mantle mostly likely reflect compositional heterogeneity and definitely influence mantle dynamics. We detect a large and spatially coherent low-velocity layer consistent with partial melting in the deep upper mantle. The inference of melting just above the transition zone carries many implications. Chief among these are the development of geochemical reservoirs through sequestration of volatiles and incompatible elements as a result of melting and the mechanical weakening of the deep upper mantle through melting and grain boundary wetting. This is an important point in time for our understanding of mantle water and its influence on mantle dynamics. Seismic data is now dense enough and of sufficient quality to detect the subtle signature of mantle water at locations around the globe. Similarly, improvements in laboratory techniques allow melting experiments to be conducted at deep upper mantle temperatures and pressures for appropriately small melt fractions (Baker et al., 1995). Water, essential to life, the shaper of Earth's surface and the lubricant of tectonics also has a role to play in the mantle. Whether that role turns out to be a cameo or a co-star may soon be known.

Acknowledgements

We thank Marc Hirschmann, Garrett Leahy, and Rajdeep Dasgupta for discussions and an anonymous reviewer for helpful suggestions. Meagan Thompson helped analyze Path 14 as part of her senior thesis project. GMT software (Wessel and Smith, 1998) was used to prepare some of the figures. This research was supported by Department of Geology and Geophysics Jensen and Murthy-Noruk fellowships (AMC) and NSF EAR-0309405.

Appendix A. Supplementary data

Supplementary data associated with this article can be found, in the online version, at doi:10.1016/j.epsl.2007.04.027.

References

Akaike, H., 1974. A new look at the statistical model identification. IEEE Trans. Automat. Contr. 19, 716–723.

Akaogi, M., Ito, E., Navrotsky, A., 1989. Olivine-modified spinel–spinel transitions in the system Mg_2SiO_4–Fe_2SiO_4: calorimetric measurements, thermochemical calculation, and geophysical application. J. Geophys. Res. 94, 15,671–15,685.

Anderson, D.L., 1989. Theory of the Earth. Blackwell Sci. Publ, Boston, MA, United States (USA).

Auzende, J., Pelletier, B., Lafoy, Y., 1994. Twin active spreading ridges in the North Fiji Basin (Southwest Pacific). Geology 22, 63–66.

Baker, M.B., Hirschmann, M.M., Ghiorso, M.S., Stolper, E.M., 1995. Compositions of near-solidus peridotite melts from experiments and thermodynamic calculations. Nature 375, 308–311.

Bell, D.R., Rossman, G.R., 1992. Water in Earth's mantle: the role of nominally anhydrous minerals. Science 255, 1391–1397.

Bercovici, D., Karato, S., 2003. Whole-mantle convection and the transition-zone water filter. Nature 425, 39–44.

Blackman, D.K., Kendall, J.-M., 1997. Sensitivity of teleseismic body waves to mineral texture and melt in the mantle beneath a mid-ocean ridge. Philos. Trans. R. Soc. Lond., A 355, 217–231.

Bolfan-Casanova, N., Keppler, H., Rubie, D.C., 2000. Water partitioning between nominally anhydrous minerals in the MgO–SiO_2–H_2O system up to 24 GPa: implications for the distribution of water in the Earth's mantle. Earth Planet. Sci. Lett. 182, 209–221.

Bolfan-Casanova, N., Keppler, H., Rubie, D.C., 2003. Water partitioning at 660 km depth and evidence for very low water solubility in magnesium silicate perovskite. Geophys. Res. Lett. 30, 17. doi:10.1029/2003GL017182.

Bolfan-Casanova, N., Kleppe, A.K., Welch, M.D., Wright, K., 2005. Water in the Earth's mantle: protons in minerals. Mineral. Mag. 69, 229–257.

Bulau, J.R., Waff, H.S., Tyburczy, J.A., 1979. Mechanical and thermodynamic constraints on fluid distribution in partial melts. J. Geophys. Res. 84, 6102–6108.

Chen, J., Inoue, T., Yurimoto, H., Weidner, D.J., 2002. Effect of water on olivine–wadsleyite phase boundary in the $(Mg, Fe)_2SiO_4$ system. Geophys. Res. Lett. 29, 10. doi:10.1029/2001GL014418.

Cmiral, M., Fitz Gerald, J.D., Faul, U.H., Green, D.H., 1998. A close look at dihedral angles and melt geometry in olivine–basalt aggregates: a TEM study. Contrib. Mineral. Petrol. 130, 336–345.

Courtier, A.M., Revenaugh, J., 2006. A water-rich transition zone beneath the eastern United States and Gulf of Mexico from ScS reverberations. In: Jacobsen, S.D., Van der Lee, S. (Eds.), Earth's Deep Water Cycle, Geophysical Monograph Series, 168, pp. 181–193.

Dalton, J.A., Presnall, D.C., 1998. Carbonatitic melts along the solidus of model lherzolite in the system CaO–MgO–Al_2O_3–SiO_2–CO_2 from 3 to 7 GPa. Contrib. Mineral. Petrol. 131, 123–135.

Dasgupta, R., Hirschmann, M.M., 2006. Melting in the Earth's deep upper mantle caused by carbon dioxide. Nature 440, 659–662.

Dasgupta, R., Hirschmann, M.M., Withers, A.C., 2004. Deep global cycling of carbon constrained by the solidus of anhydrous, carbonated eclogite under upper mantle conditions. Earth Planet. Sci. Lett. 227, 73–85.

Dobson, D.P., Jones, A.P., Rabe, R., Sekine, T., Kurita, K., Taniguchi, T., Kondo, T., Kato, T., Shimomura, O., Urakawa, S., 1996. In-situ measurement of viscosity and density of carbonate melts at high pressure. Earth Planet. Sci. Lett. 143, 207–215.

Dziewonski, A.M., Anderson, D.L., 1981. Preliminary reference Earth model. Phys. Earth Planet. Inter. 25, 297–356.

Eggler, D.H., 1976. Does CO_2 cause partial melting in the low-velocity layer of the mantle? Geology 4, 69–72.

Flanagan, M.P., Shearer, P.M., 1998. Global mapping of topography on transition zone velocity discontinuities by stacking SS precursors. J. Geophys. Res. 103, 2673–2692.

Gilbert, H.J., Sheehan, A.F., Dueker, K.G., Molnar, P., 2003. Receiver functions in the western United States, with implications for upper mantle structure and dynamics. J. Geophys. Res. 108. doi:10.1029/2001JB001194.

Green, H.W., 1972. A CO_2 charged asthenosphere. Nature 238, 2–5.

Hall, R., Spakman, W., 2003. Mantle structure and tectonic evolution of the region north and east of Australia: evolution and dynamics of the Australian Plate. Spec. Pap. - Geol. Soc. Am. 372, 361–381.

Helffrich, G.R., Wood, B.J., 1996. 410 km discontinuity sharpness and the form of the olivine alpha–beta phase diagram: resolution of apparent seismic contradictions. Geophys. J. Int. 126, F7–F12.

Hier-Majumder, S., Ricard, Y., Bercovici, D., 2006. Role of grain boundaries in magma migration and storage. Earth Planet. Sci Lett. 248, 735–749.

Higo, Y., Inoue, T., Irifune, T., Yurimoto, H., 2001. Effect of water on the spinel–postspinel transformation in Mg_2SiO_4. Geophys. Res. Lett. 28, 3505–3508.

Hirschmann, M.M., Aubaud, C., Withers, A.C., 2005. Storage capacity of H_2O in nominally anhydrous minerals in the upper mantle. Earth Planet. Sci. Lett. 236, 167–181.

Hirschmann, M.M., Withers, A.C., Aubaud, C., 2006. Petrologic structure of a hydrous 410 km discontinuity. In: Jacobsen, S.D., Van der Lee, S. (Eds.), Earth's Deep Water Cycle, Geophysical Monograph Series, 168, pp. 277–287.

Ingrin, J., Skogby, H., 2000. Hydrogen in nominally anhydrous upper-mantle minerals: concentrations levels and implications. Eur. J. Mineral. 12, 543–570.

Inoue, T., Weidner, D.J., Northrup, P.A., Parise, J.B., 1998. Elastic properties of hydrous ringwoodite (gamma-phase) in Mg_2SiO_4. Earth Planet. Sci. Lett. 160, 107–113.

Irifune, T., Ringwood, A.E., 1993. Phase transformations in subducted oceanic crust and buoyancy relationships at depths of 600–800 km in the mantle. Earth Planet. Sci. Lett. 117, 101–110.

Irifune, T., Kubo, N., Isshiki, M., Yamasaki, Y., 1998. Phase transformations in serpentine and transportation of water into the lower mantle. Geophys. Res. Lett. 25, 203–206.

Ito, E., Takahashi, E., 1989. Postspinel transformations in the system Mg_2SiO_4–Fe_2SiO_4 and some geophysical implications. J. Geophys. Res. 94, 10,637–10,646.

Karato, S.-I., Bercovici, D., Leahy, G., Richard, G., Jing, Z., 2006. The transition-zone water filter model for global material circulation: where do we stand? In: Jacobsen, S.D., Van der Lee, S. (Eds.), Earth's Deep Water Cycle, Geophysical Monograph Series, 168, pp. 289–313.

Katayama, I., Nakashima, S., 2003. Hydroxyl in clinopyroxene from the deep subducted crust: evidence for H_2O transport into the mantle. Am. Mineral. 88, 229–234.

Kendall, J.M., Shearer, P.M., 1995. On the structure of the lowermost mantle beneath the Southwest Pacific, Southeast Asia and

Australasia: structure, composition and evolution of the Earth's interior. Phys. Earth Planet. Inter. 92, 85–98.
Keppler, H., 2003. Water solubility in carbonatite melts. Am. Mineral. 88, 1822–1824.
Keppler, H., Wiedenbeck, M., Shcheka, S.S., 2003. Carbon solubility in olivine and the mode of carbon storage in the Earth's mantle. Nature 424, 414–416.
Kohlstedt, D.L., Keppler, H., Rubie, D.C., 1996. Solubility of water in the alpha, beta and gamma phases of $(Mg,Fe)_2SiO_4$. Contrib. Mineral. Petrol. 123, 345–357.
Leahy, G.M., Bercovici, D., in press. On the dynamics of a hydrous melt layer above the transition zone. J. Geophys. Res. doi:10.1029/2006JB004631.
Matsukage, K.N., Jing, Z., Karato, S., 2005. Density of hydrous silicate melt at the conditions of Earth's deep upper mantle. Nature 438, 488–491.
Minarik, W.G., Watson, E.B., 1995. Interconnectivity of carbonate melt at low melt fraction. Earth Planet. Sci. Lett. 133, 423–437.
Murakami, M., Hirose, K., Yurimoto, H., Nakashima, S., Takafuji, N., 2002. Water in Earth's lower mantle. Science 295, 1885–1887.
Neuberg, J., Wahr, J.M., 1991. Detailed investigation of a spot on the core–mantle boundary using digital PcP data: studies of the Earth's deep interior. Phys. Earth Planet. Inter. 68, 132–143.
Ohtani, E., Nagata, Y., Suzuki, A., Kato, T., 1995. Melting relations of peridotite and the density crossover in planetary mantles: chemical evolution of the mantle. Chem. Geol. 120, 207–221.
Parson, L.M., Wright, I.C., 1996. The Lau–Havre–Taupo back-arc basin: a southward-propagating, multi-stage evolution from rifting to spreading. Tectonophysics 263, 1–22.
Pino, N.A., Helmberger, D.V., 1997. Upper mantle compressional velocity structure beneath the West Mediterranean Basin. J. Geophys. Res. 102, 2953–2967.
Revenaugh, J., Jordan, T.H., 1989. A study of mantle layering beneath the western Pacific. J. Geophys. Res. 94, 5787–5813.
Revenaugh, J., Jordan, T.H., 1991a. Mantle layering from ScS reverberations: 1. Waveform inversion of zeroth-order reverberations. J. Geophys. Res. 96, 19,749–19,762.
Revenaugh, J., Jordan, T.H., 1991b. Mantle layering from ScS reverberations: 2. The transition zone. J. Geophys. Res. 96, 19,763–19,780.
Revenaugh, J., Jordan, T.H., 1991c. Mantle layering from ScS reverberations: 3. The upper mantle. J. Geophys. Res. 96, 19,781–19,810.
Revenaugh, J., Sipkin, S.A., 1994. Seismic evidence for silicate melt atop the 410-km mantle discontinuity. Nature 369, 474–476.
Sakamaki, T., Suzuki, A., Ohtani, E., 2006. Stability of hydrous melt at the base of the Earth's upper mantle. Nature 439, 192–194.
Sdrolias, M., Mueller, R.D., Gaina, C., 2003. Tectonic evolution of the Southwest Pacific using constraints from backarc basins: evolution and dynamics of the Australian Plate. Spec. Pap. - Geol. Soc. Am. 372, 343–359.
Shieh, S.R., Mao, H., Hemley, R.J., Ming, L.C., 1998. Decomposition of phase D in the lower mantle and the fate of dense hydrous silicates in subducting slabs. Earth Planet. Sci. Lett. 159, 13–23.
Smith, C.S., 1964. Some elementary principles of polycrystalline microstructure. Metall. Rev. 9, 1–48.
Smyth, J.R., Frost, D., 2002. The effect of water on the 410-km discontinuity: an experimental study. Geophys. Res. Lett. 29, 10. doi:10.1029/2001GL014418.
Song, T.R.A., Helmberger, D.V., Grand, S.P., 2004. Low-velocity zone atop the 410-km seismic discontinuity in the northwestern United States. Nature 427, 530–533.
Stevenson, D.J., 1986. On the role of surface tension in the migration of melts and fluids. Geophys. Res. Lett. 13, 1149–1152.
Stolper, E., Walker, D., Hager, B.H., Hays, J.F., 1981. Melt segregation from partially molten source regions: the importance of melt density and source region size. J. Geophys. Res. 86, 6261–6271.
Tatsumi, Y., 1989. Migration of fluid phases and genesis of basalt magmas in subduction zones. J. Geophys. Res. 94, 4697–4707.
Taylor, B., Zellmer, K., Martinez, F., Goodliffe, A.M., 1996. Sea-floor spreading in the Lau back-arc basin. Earth Planet. Sci. Lett. 144, 35–40.
Van der Meijde, M., van der Lee, S., Giardini, D., 2005. Seismic discontinuities in the Mediterranean mantle. Phys. Earth Planet. Inter. 148, 233–250.
Vinnik, L., Farra, V., 2002. Subcratonic low-velocity layer and flood basalts. Geophys. Res. Lett. 29, 4. doi:10.1029/2001GL014064.
Vinnik, L., Kumar, M.R., Kind, R., Farra, V., 2003. Super-deep low-velocity layer beneath the Arabian Plate. Geophys. Res. Lett. 30, 7. doi:10.1029/2002GL016590.
Wessel, P., Smith, W.H.F., 1998. New, improved version of the Generic Mapping Tools released. EOS Trans. AGU 79, 579.
Wood, B.J., 1995. The effect of H_2O on the 410-kilometer seismic discontinuity. Science 268, 74–76.
Wyllie, P.J., Huang, W., 1976. Carbonation and melting reactions in the system $CaO–MgO–SiO_2–CO_2$ at mantle pressures with geophysical and petrological applications. Contrib. Mineral. Petrol. 54, 79–107.
Yoshino, T., Nishihara, Y., Karato, S.-I., 2007. Complete wetting of olivine grain boundaries by a hydrous melt near the mantle transition zone. Earth Planet. Sci. Lett. 256, 466–472.